J. Phys. Chem. B **2006,** *110,* 19945−19955

Photoionization and Photofragmentation of SF_6 in Helium Nanodroplets[†]

Darcy S. Peterka, Jeong Hyun Kim, Chia C. Wang, and Daniel M. Neumark*

Department of Chemistry, University of California, Berkeley, California 94720, and Chemical Sciences Division, Lawrence Berkeley National Laboratory, Berkeley, California 94720

Received: April 8, 2006; In Final Form: June 1, 2006

The photoionization of He droplets doped with SF_6 was investigated using tunable vacuum ultraviolet (VUV) synchrotron radiation from the Advanced Light Source (ALS). The resulting ionization and photofragmentation dynamics were characterized using time-of-flight mass spectrometry combined with photofragment and photoelectron imaging. Results are compared to those of gas-phase SF_6 molecules. We find dissociative photoionization to SF_5^+ to be the dominant channel, in agreement with previous results. Key new findings are that (a) the photoelectron spectrum of the SF_6 in the droplet is similar but not identical to that of the gas-phase species, (b) the SF_5^+ photofragment velocity distribution is considerably slower upon droplet photoionization, and (c) fragmentation to SF_4^+ and SF_3^+ is much less than in the photoionization of bare SF_6. From these measurements we obtain new insights into the mechanism of SF_6 photoionization within the droplet and the cooling of the hot photofragment ions produced by dissociative photoionization.

1. Introduction

This paper presents a study of the photoionization of He nanodroplets doped with SF_6 and the photofragmentation and photoelectron dynamics resulting from this process. This work is motivated by our desire to understand the interaction of charged particles with the weakly interacting but relatively dense solvent atoms in a He droplet. While there have been many infrared and electronic spectroscopy experiments that have probed the interaction of neutral particles with He nanodroplets,[1−3] the stronger interactions expected for charged species (either ions or electrons) produced in droplets remain largely unexplored and certainly not well understood. For example, photoelectron imaging experiments performed on pure He droplets at energies below the ionization potential of atomic He showed exceedingly slow photoelectrons, with an average energy below 1 meV,[4] while analogous experiments on droplets doped with aniline yielded photoelectron kinetic energies that were higher than those seen for bare aniline.[5] Hence, the two experiments show evidence for significant but very different electron−solvent interactions. The experiments presented here offer further insight into the dynamics of charged particles in droplets.

The motion of particles and dissipation of energy in liquid helium has been of interest for many years. Experiments in bulk liquid helium have shown that impurities moving below a critical speed can do so with little energy dissipation. The low-speed motion of ions in bulk liquid helium is well understood.[6−8] At liquid temperatures below 0.8 K and small drift velocities, ions under the influence of an electric field move with a speed proportional to the electric field, with low-energy phonon scattering being the dissipation mode. At slightly higher liquid helium temperatures (<1.5 K), ions with low drift velocities scatter against thermally excited rotons in the fluid, and the mobility becomes inversely proportional to the roton density. At speeds higher than the Landau critical velocity ($\sim$58 m s^{-1}) ion−helium collisions can create high-energy excitations directly, and the ion experiences friction.

In helium droplets, despite great interest, there is a dearth of experimental studies on translational motion of impurities. Crossed-beam scattering has revealed some details on atoms and molecules traversing the droplets,[9,10] but the information is indirect. Dispersed fluorescence experiments have shown that intrinsic impurities can traverse and escape the droplet.[11] A recent study created moving neutral impurities within the droplet with well-defined kinetic energy and gave direct evidence of translational energy dissipation in the droplet.[12]

The above experiments were conducted with neutral impurities, where the interaction between the dopant and surrounding helium is expected to be weak. With ions, the situation may be different. In the bulk, ions are well-known to make “snowballs”.[13−15] The snowballs are comprised of the ion core and a dense shell of helium atoms. The snowball is created primarily because of the ion-induced dipole attraction between the ion and neighboring helium atoms:

$$V(r) = \frac{-\alpha e^2}{32\pi^2 \epsilon_r^{\,2} r^4}$$

with α being the polarizability of the helium atoms and ϵ_r being the density-dependent dielectric constant. In bulk, most of the experiments on the motion of ions measure the motion of the entire snowball, not that of the bare ion, and only small differences are seen between different ion cores.[16] The ion is either injected into the liquid, or for intrinsic impurities (i.e., He^+ or He_2^+), created with a fast-moving charged projectile. The details of the initial ionization and excitation have very little effect on the final state, however, as the macroscopic liquid helium environment can completely dissipate any electronic excitation and the initial translational energy of the impurity quickly on the time scale of the experiments. Bulk liquid helium also has essentially infinite heat capacity and extent relative to

---

[†] Part of the special issue “Charles B. Harris Festschrift”.

* Corresponding author. Phone: 510-642-3502. Fax: 510-642-3635. E-mail: dneumark@berkeley.edu.

10.1021/jp062195o CCC: $33.50

those of the microscopic dopant, and the snowball has time to form and be equilibrated to the bulk temperature.

For very large droplets ($>10^8$ atoms), the ions can equilibrate, and the situation is like that of the bulk.[17,18] For smaller droplets ($<10^5$ atoms), the finite size may significantly alter the formation of the ion and alter the dynamics of ion motion. In most droplet experiments, ions are formed from neutral species inside the droplet, typically the result of an excitation transfer between He^+ (or other He_n^+ species) and the dopant.[9,19−22] For static ions, that is, ions formed with little initial kinetic energy, experiments using electron impact ionization or photoionization see results consistent with the stronger ion−helium interaction.[20,21,23] In many of the mass spectra from doped droplets, $X^+\cdot He_n$ ions are common. In some experiments, $X^+\cdot He_{12}$ ions are prominent;[21,24] this ion complex corresponds to the dopant ion surrounded by a completed F. C. C helium shell. The excitation transfer leading to ionization of the dopant is highly exothermic, and for small to medium size droplets ($<5 \times 10^4$ atoms), the resulting energy release usually results in the partial destruction of the droplet—one sees only smaller cluster ions.

The fragmentation process requires energy, and is associated with some cooling within the droplet. Recent experiments in the Miller group on the cooling of the triphenyl methanol ion following electron impact ionization allowed for a more quantitative study of the cooling.[25] They fit their gas-phase breakdown pattern with RRKM theory and were able to estimate a rate constant for unimolecular dissociation of the ion. The rate plateaued near 10^{11} s^{-1} for the highest electron impact energies. For the helium droplet to be effective in suppressing fragmentation, they noted that the cooling rate should be at least of comparable magnitude.

Similar results on the cooling of ions were indicated in earlier studies of SF_6-doped droplets by Toennies' group.[19] Experiments using electron impact ionization of SF_6-doped helium droplets indicated a strong suppression of the smaller SF_k^+ ions, with preferential production of SF_5^+. A small amount of SF_6^+ ion was also apparently seen. It was assumed that the appearance of this ion was the result of very efficient cooling of the SF_6^+ ion within the droplet along with possible steric interference—caging—of the outgoing fragments. On this observation and the relative ratio of SF_5^+/SF_6^+, the authors calculated an effective cooling rate in the droplet estimated to be $\sim 10^{16}$ K s^{-1}. However, later experiments in the same group failed to detect any SF_6^+ from SF_6-doped droplets,[26] calling the cooling results into question.

In this paper, the photoionization of He droplets doped with SF_6 was investigated using tunable vacuum ultraviolet (VUV) synchrotron radiation from the Advanced Light Source (ALS). The resulting ionization and photofragmentation dynamics were characterized using time-of-flight mass spectrometry combined with photofragment and photoelectron imaging. Results are compared with a similar study of bare SF_6 molecules. We find dissociative photoionization to SF_5^+ to be the dominant channel, in agreement with Toennies. Key new findings are that (a) the photoelectron spectrum of the SF_6 in the droplet is similar but not identical to that of the bare ion, (b) the SF_5^+ photofragment velocity distribution is considerably slower upon droplet photoionization, and (c) fragmentation to SF_4^+ and SF_3^+ is much less than in the photoionization of bare SF_6. From these measurements we obtain new insights into the mechanism of SF_6 photoionization within the droplet and the cooling of the hot photofragment ions produced by dissociative photoionization.

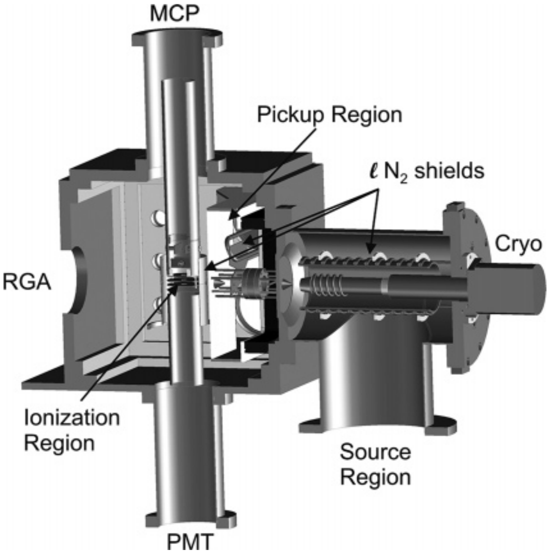

Figure 1. Helium droplet machine schematic.

2. Experimental Section

A schematic of the machine is illustrated in Figure 1. The helium cluster beam was produced by expanding high-pressure, high-purity (99.9995%) helium through a 5 μm diameter orifice mounted on the second stage of a closed cycle helium refrigerator (ARS 204-FF with 6 K option). The helium gas was filtered through a 0.5 μm sintered filter and precooled to 77 K by circulating it around a 2×10^3 cm^2 liquid nitrogen cooled shroud that also served to shield the nozzle and cryopump the source chamber. Droplet size was controlled by adjusting the temperature and pressure of the source; the experiments described here were conducted with 60 bar backing pressure and $\sim$16 K nozzle temperature, resulting in droplets with $\langle N \rangle \approx 10\,000$. The source chamber was pumped by a 3200 L s^{-1} magnetically levitated turbopump (Osaka TG 3213EM). With no helium flowing, the base pressure was $\sim 1 \times 10^{-8}$ torr; under typical beam conditions the source region pressure was 1×10^{-4} torr (IG uncorrected).

The pickup region contained a 5 cm long pickup cell with 2.5 mm apertures. The pressure was controlled by a variable rate precision leak valve and monitored by an ion gauge directly mounted to the pickup cell. A beam flag could block the droplet beam before the gas cell's entrance aperture. The pickup region was pumped by a 400 L s^{-1} magnetically levitated turbo pump (Seiko Seiki TMP400) backed by an oil-free scroll pump. In addition, a 300 cm^2 liquid nitrogen cooled cryopanel located in this chamber removed residual H_2O or any other volatile species. The helium cluster beam exited into the main chamber through a 2 mm skimmer (Beam Dynamics). When the cell was not being used and the helium beam off, the base pressure of the pickup chamber was 5×10^{-9} torr.

In the main chamber, the helium beam crossed the VUV photon beam on the axis of our time-of-flight (TOF)/imaging spectrometer. The interaction region and the lower portions of the spectrometer were surrounded by a liquid nitrogen cooled cylinder (total surface area 1.4×10^3 cm^2) with four 1 cm holes around the perimeter, which allowed the helium beam and the VUV beam passage. For offline diagnostics, a residual gas analyzer (SRS RGA 200) intersected the helium beam 30 cm downstream of the interaction region. The base pressure in the main chamber was $\sim 5 \times 10^{-9}$ torr. The expected probability of the cluster inadvertently picking up an impurity along its path was $<1\%$.

Three types of experiments are reported here: time-of-flight mass spectrometry, mass-selected ion photofragment imaging, and photoelectron imaging. The electron optical setup for photoelectron imaging has been described previously.[4] For the time-of-flight mass spectrometer measurements (TOF-MS), the ion optics consisted of a Wiley−McLaren[27] style lens stack composed of a repeller mesh, an accelerator mesh, and a grounded mesh. The repeller plate was pulsed ~300 V above the accelerator to extract the ions and provide t_0. The 0.8 m flight tube contained two matched pairs of deflection plates and an Einzel lens for optimal steering and focusing of the ion packet onto the detector. The detector assembly was a resistance-matched pair of 40 mm microchannel plates coupled to a conical anode. A high-speed multichannel scaler recorded the TOF spectrum (500 ps per bin, FASTComtec P7886). Typical mass spectra reported here were accumulated for 2^{19} to 2^{23} sweeps with mass resolution $(M/\Delta M) = 400$.

For the mass-selected ion imaging results, a similar pulsing scheme was used but with a Wiley−McLaren stack coupled to a velocity-mapped imaging lens system. The complete system comprised a pair of electrodes with flat 93% transmissive grids to perform the initial ion extraction, immediately followed by a conventional velocity map lens system. This hybrid arrangement was necessary because pulsed extraction using only the velocity map system led to poor TOF resolution. The additional velocity map lens system allowed for significant removal of the spatial blurring present in a typical Wiley−McLaren imaging setup. A small spoiling field was also used to prevent any buildup of ions with v_{lab} near zero, which could skew our observations. The ions were detected by an 80 mm MCP detector assembly coupled to a phosphor screen (Burle APD 3075FM). The MCP bias voltage was pulsed high for 200 ns to gate on the ion of choice. The phosphor screen was imaged with a 1 megapixel CCD camera (DALSA 1M30) and integrated on a PC. The images, 2-D projections of the full 3-D product ion distribution, were reconstructed with well-established tomographic methods.[28,29] The spoiling field and pulsing scheme unfortunately do not provide perfect imaging conditions and introduce some uncertainty in the absolute velocities derived from the images; however, we estimate these uncertainties to be <15%, and they do not affect the interpretation. The mass resolution in the ion imaging experiments was ~30. The photoelectron images were acquired with a standard velocity map imaging lens system.[30]

VUV light was provided by Terminal 3 of the Chemical Dynamics Beamline at the ALS, a third-generation synchrotron light source. At the Chemical Dynamics Beamline, an undulator provides $\sim 10^{16}$ photons s^{-1} (2.5% bandwidth) of linearly polarized light from 7 to 30 eV.[31] Terminal 3 consists of a 3m off-plane Eagle monochromator fitted with a 600 lines/mm grating and a best possible energy resolution $(E/\Delta E) \approx 3000$. For these experiments, an Ir-coated master grating blazed for 16 eV was used, and the monochromator was set to provide $E/\Delta E \approx 600$, yielding 10^{13} photons s^{-1} in the range of 20−26 eV. The light is pseudocontinuous, with a repetition rate of 500 MHz.

In both TOF and imaging measurements, further modulation of the light beam was required. Simple pulse extraction methods give satisfactory, but not ideal, results when the light beam is nearly continuous. Ions formed late in the voltage pulse do not leave the extraction region before the field collapses, giving rise to an energy spread in the ion packet. The TOF peaks then have long tails extending to later flight times, potentially obscuring small, nearby higher mass peaks and greatly diminishing the effective dynamic range of the experiment. This is especially important when examining species from helium droplets, when there may be small amounts of $X^+ \cdot He_n$ next to large X^+ signals, such as in the experiments described here. At the Chemical Dynamics Beamline, a fast chopper was installed to address this problem. It consists of a custom-built in vacuo motor capable of rotation speeds up to 1000 Hz, coupled to a 12.5 cm diameter wheel with slot patterns photoetched near the outer rim. During our experiments, the chopper provided light pulses with 10−90% rise times of less than 1 μs, a 90−90% time of 12 μs, and a repetition rate of ~32 kHz. Because some of the flight times in the experiment were greater than $1/f_{\mathrm{chop}}$, we chose to extract the ions only on every other light pulse, rather than slow the wheel, which would lengthen the rise and fall times. The ion extraction pulse was triggered to coincide with the falling edge of a light pulse in the ionization region.

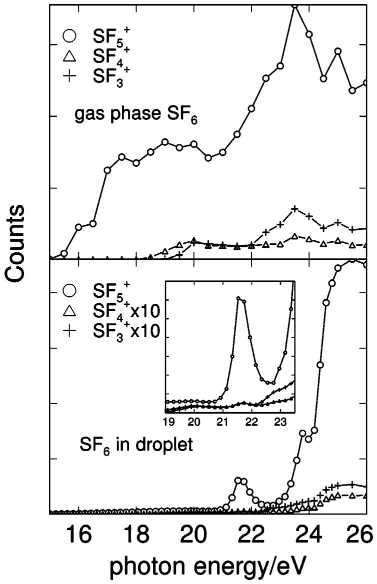

Figure 2. Normalized ion yield of (top) gas-phase sulfur hexafluoride, SF_{6gp}, and (bottom) sulfur hexafluoride doped in helium droplets, SF_{6drop}. In the droplet data, the SF_4^+ and SF_3^+ are shown scaled by 10× for visibility. The inset shows the zoom of the region from 19 to 23.5 eV.

Our gas-phase spectra were taken by blocking the helium cluster beam before the pickup cell, and then increasing the pickup cell pressure to a high value, with the cell then acting as an effusive source. Doped spectra were taken under a variety of pickup cell pressures from 2×10^{-7} to 2×10^{-4} torr. The majority of the TOF-MS results for doped droplets shown here were recorded with 1.0×10^{-5} torr in the pickup cell, which provided nearly maximal absolute count rates for the singly doped helium droplet signal without interference from multiply doped droplets. Scrutiny of the data with other results taken with pickup pressures a few times higher than the ones reported in this paper indicated no apparent differences in the ions related to single SF_6 pickup, either in the mass spectra or the images.

3. Results

Previous detailed studies of the photoabsorption and subsequent dissociation of gas-phase sulfur hexafluoride (SF_{6gp}) in the VUV have been conducted both in this group and by others,[32−38] so the results for SF_{6gp} will only be briefly summarized. The upper panel of Figure 2 shows the ion yield for dissociative photoionization of SF_{6gp} from 15 to 26 eV, obtained by integrating the appropriate peaks in the TOF mass spectrum as a function of photon energy, and is consistent with previous measurements.[32] The dominant ion seen at all energies is SF_5^+, with smaller amounts of the SF_4^+ and SF_3^+ fragments. The SF_5^+ ion appears at ~15.5 eV and rises steadily until ~18 eV, where it levels off. At 21 eV, SF_5^+ production increases again—the leading edge of a broad peak centered near 24 eV. The onsets of SF_4^+ and SF_3^+ occur at 18.5 and 19.0 eV, respectively. At 20 eV, SF_3^+ production matches SF_4^+, and the branching ratio and absolute amounts of the two ions remain nearly constant until 22 eV. Here, the SF_3^+ ion yield increases sharply, while the SF_4^+ signal remains relatively constant.

The ion yield curves for sulfur hexafluoride doped in helium droplets (SF_{6drop}) are shown in the lower panel of Figure 2. The data shown for SF_4^+ and SF_3^+ are scaled by a factor of 10 in order to be visible. As in SF_{6gp}, SF_5^+ is the prominent ion, but the ratio of SF_5^+ to the smaller SF_k^+ fragments is much higher. The curve measured for SF_5^+ is very similar to the curve measured earlier for SF_5^+ from SF_6-doped helium droplets by the Toennies group.[26] It shows a very strong peak near the He 2P atomic absorption, while SF_4^+ and SF_3^+ change very little (inset, lower panel of Figure 2). The measured SF_5^+ curve is also similar in structure to the fluorescence excitation curves for pure droplets of similar size, measured by the group of Möller.[39−41] The SF_3^+ ion increases again at 22 eV. Near 23 eV, the threshold for ionization of pure helium droplets, the signals of all SF_k^+ fragment ions rise, but with a very clear preference for SF_5^+ production.

Examining the ion channel branching ratios for SF_{6gp} excited at 21.8 eV, one finds $SF_5^+/SF_4^+ = 9.5$, $SF_5^+/SF_3^+ = 9.2$. At 25.5 eV excitation, $SF_5^+/SF_4^+ = 12$, $SF_5^+/SF_3^+ = 5.7$. For SF_{6drop}, at both 21.75 and 25.5 eV, the ratio of SF_5^+ to both SF_k^+ ($k = \{4,3\}$) is near 100:1. At energies where there is no appreciable pure droplet photoabsorption,[39−41] ~22−23 eV, the fragment ion branching ratios appear only slightly different from the gas-phase results; the SF_5^+ signal decreases, while the smaller SF_k^+ peaks remain essentially constant. Note that the data shown in the lower panel of Figure 2 are not background-subtracted. Thus, the actual ratio recorded for the droplet signal depends strongly on many mundane experimental factors, such as the background SF_{6gp}, and should be considered only as a guide. Individual background-subtracted TOF-MS indicates that virtually all of the SF_k^+ ($k = \{4,3\}$) ions seen at 21.8 eV in the doped spectra are from the effusive SF_{6gp} background and not associated with SF_{6drop}. This means that at 21.8 eV there is a very large increase in SF_5^+ while the droplet beam is on and almost no change in either SF_4^+ or SF_3^+. The corrected spectra at 25.5 eV show similar effects, but at this energy, some of the detected SF_3^+ and SF_4^+ fragments correlate with SF_{6drop}.

Closer examination of the individual TOF-MS spectra in Figures 3−5 yields additional information. The highest mass shown in these figures is 200 amu, but the recorded spectra extended to 1200 amu, and the presence or absence of features in this extended range will be noted when applicable. Parts a−c of Figure 3 show TOF-MS spectra of SF_{6drop} at 21.8 eV at various levels of detail. In Figure 3a, the peaks at 89 (SF_3^+) and 108 (SF_4^+) amu are dwarfed by the peak at 127 (SF_5^+) amu. Figure 3b shows that toward heavier masses there is a progression of peaks with mass 127 + 4*n* ($SF_5^+\cdot He_n$), contrary to earlier studies where no $SF_5^+\cdot He_n$ was detected, presumably owing to lower resolution and lower signal-to-noise in the earlier experiments.[19,26] This progression decreases in intensity as it extends toward higher masses and is present in the extended mass spectra to $n = 25$, after which the S/N is too low for definitive assignment. There is no evidence of any $SF_k^+\cdot He_n$ for $k = \{4,3\}$. A small peak is seen at 164 amu ($SF_6\cdot H_2O^+$). The peak at 175 amu ($SF_5^+\cdot He_{12}$), the expected "magic number" for helium, shows no sign of enhanced intensity compared with its $\Delta m \pm 4$ neighbors. Figure 3c shows that there are clear peaks at 145 ($SF_5\cdot H_2O^+$, $^{34}SF_5^+\cdot He_4$) and 147 amu ($^{34}SF_5\cdot H_2O^+$, $SF_5^+\cdot He_5$), but there is no detectable signal at 146 amu (SF_6^+). With increasing pickup pressure, $SF_5^+\cdot(SF_6)_n$ cluster ions are seen as well.

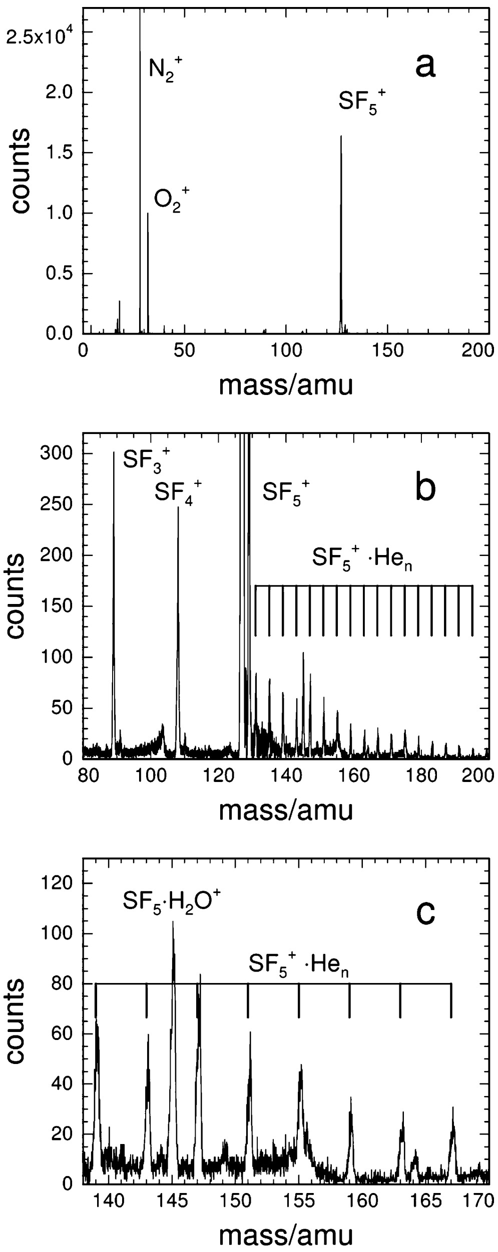

Figure 3. TOF-MS following 21.8 eV excitation of SF_6-doped helium droplets. (a) A large SF_5^+ peak is seen with little SF_4^+ or SF_3^+. The N_2 and O_2 signals are from background gas in the ionization region and do not depend on the droplet beam. (b) A close up look of the SF_6-dependent region. After the SF_5^+ a progression of $SF_5^+\cdot He_n$ is seen. (c) $SF_5^+\cdot He_n$ and $SF_5^+H_2O^+$ but no SF_6^+.

Excitation at 25.5 eV leads to similar results, with some additional features observed (Figure 4). The largest ion signal is mass 4 (He^+), and is followed by a series of peaks of mass 4*n*. Similar differences at the two photon energies were seen in the photoionization mass spectra of droplets doped with rare gas atoms.[24] In Figure 4, SF_5^+ is still the dominant heavy ion. Again, there is a series of peaks corresponding to $SF_5^+\cdot He_n$ extending the length of the figure (in the full TOF-MS, the He_n^+ peaks are visible to $n \sim 80$ while the $SF_5^+\cdot He_n$ peaks continue to $n > 40$). With the stronger overall signal, peaks related to

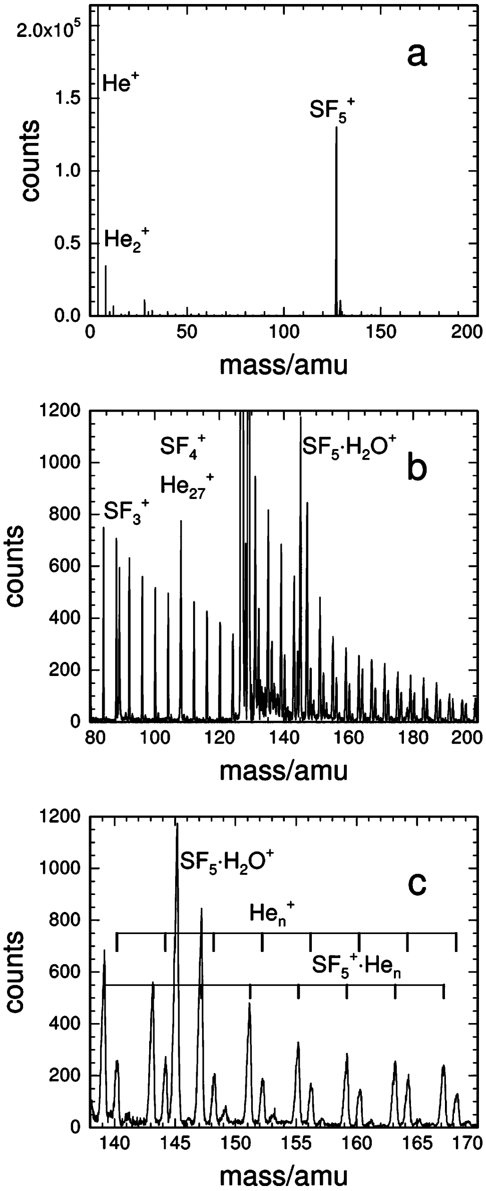

Figure 4. TOF-MS following 25.5 eV excitation of SF_6-doped helium droplets. (a) A large SF_5^+ peak is seen with little SF_4^+ or SF_3^+. (b) A close up look of the SF_6-dependent region. Now the pure helium cluster ion signals are seen. After the SF_5^+ a progression of $SF_5^+ \cdot He_n$ is seen. (c) $SF_5^+ \cdot He_n$ and $SF_5^+H_2O^+$ but no SF_6^+.

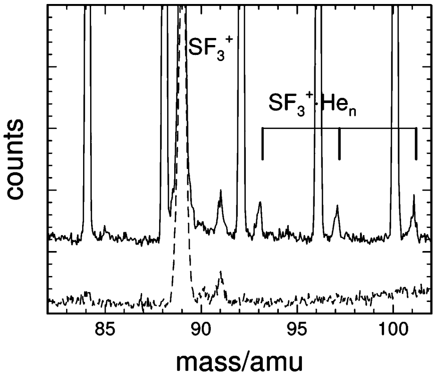

Figure 5. Upper solid trace shows the formation of $SF_3^+ \cdot He_n$ from the SF_6-doped droplet beam following 25.5 eV photoexcitation. The $SF_3^+ \cdot He_n$ peaks are absent in the lower dashed trace, which is from the SF_6-doped droplet beam following 21.8 eV excitation.

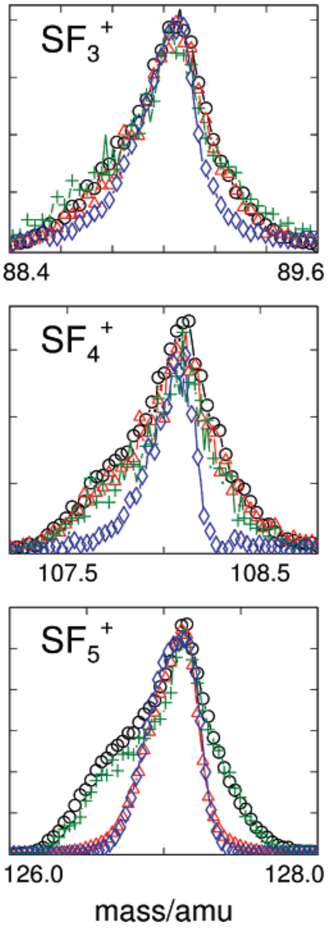

Figure 6. TOF narrowing. The spectra are all normalized, so the effects can be clearly seen: black circles, 21.8 eV gas-phase SF_6; red triangles, 21.8 eV SF_6 in droplets; green crosses, 25.5 eV gas-phase SF_6; blue diamonds, 25.5 eV SF_6 in droplets. The SF_4^+ spectra at 25.5 eV excitation are corrected by subtracting the estimated He_{27}^+ contribution.

$^{34}SF_5^+ \cdot He_n$ and $^{33}SF_5^+ \cdot He_n$, are also visible, although the latter is very weak. The peak at 164 amu ($SF_6 \cdot H_2O^+$) is slightly higher than its $\Delta m \pm 4$ neighbors. The peaks at 145 and 147 amu are now even more prominent. A very weak signal is present at 146 amu, possibly SF_6^+, though its intensity is 1×10^5 times less than that of mass 127, and may be attributable to ($^{33}SF_5 \cdot H_2O^+$). At 25.5 eV excitation, with increasing pickup pressure, in addition to $SF_5^+ \cdot (SF_6)_n$ cluster ions, the smaller $SF_k^+ \cdot (SF_6)_n$ ions are also seen.

Figure 5 shows a detail of the TOF-MS around the SF_3^+ peak at 25.5 and 21.8 eV. At the higher energy, a progression of peaks is seen at masses $89 + 4n$, corresponding to $SF_3^+ \cdot He_n$. It continues clearly up to $SF_3^+ \cdot He_9$, after which the signal is obscured by the strong signals related to $^{34}SF_5^+$. As pure helium cluster ions overlap with the $SF_4^+ \cdot He_n$ ions, we cannot directly confirm the presence of $SF_4^+ \cdot He_n$ ions, though they are likely present.

Figure 6 compares peak widths of SF_k^+ ions from TOF-MS of bare and clustered SF_6 at 21.8 and 25.5 eV. At 21.8 eV the relative width of the SF_5^+ droplet peak is narrower than in the gas-phase spectra, while not surprisingly, the widths of masses 89 and 108 are unchanged. At 25.5 eV excitation, however, the peaks of all of the SF_k^+ ions from droplets are narrowed relative to those of SF_{6gp}, with SF_5^+ showing the largest effect. This modulation of peak width is useful and will be used later as an aid in the interpretation of the dynamics of fragmentation and escape of the ions.

Figure 7 displays representative photofragment images SF_5^+ produced from SF_{6gp} and SF_{6drop}. Each image is independently

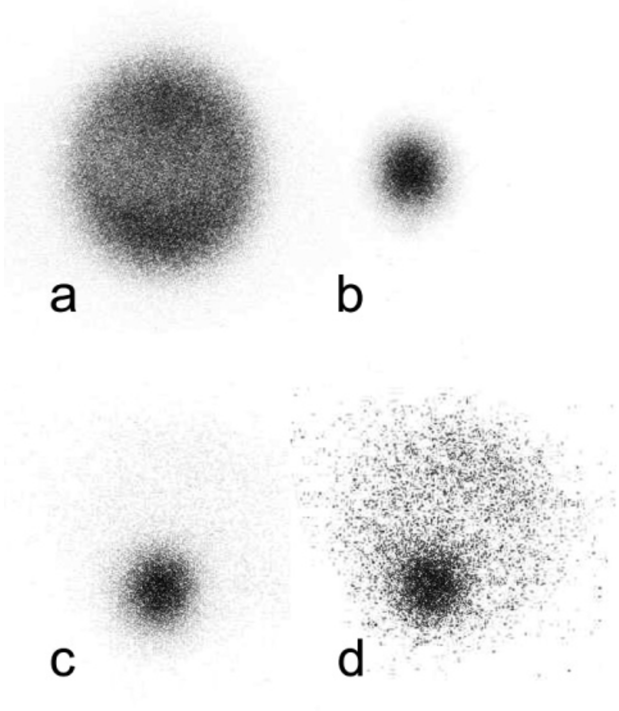

Figure 7. Normalized SF_5^+ ion images. (a) SF_5^+ from gas-phase SF_6 at 25.5 eV excitation. (b) SF_5^+ from the helium droplet at 25.5 eV. (c) SF_5^+ from the droplet at 21.8 eV. (d) Log-scale image of SF_5^+ from the droplet at 22.8 eV. All of the $SF_5^+{}_{drop}$ images show similar behavior and are slowed markedly compared to those of the $SF_5^+{}_{gp}$ results.

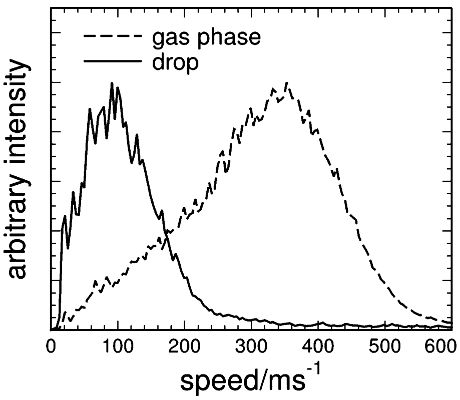

Figure 8. Fragment speed distributions: $SF_5^+{}_{drop}$ and $SF_5^+{}_{gp}$ following 25.5 eV excitation. The dashed line shows the gas-phase results, while the solid line shows the droplet data. The results for 21.8 eV are identical within the resolution of the experiment.

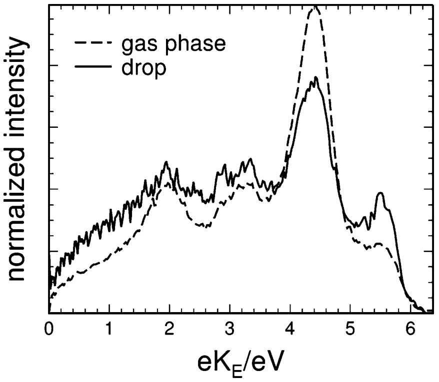

Figure 9. Electron kinetic energy spectra following 21.8 eV excitation. Spectra are normalized to the total integrated intensity. The dashed line shows the gas-phase SF_6 spectrum, and the solid line shows the spectrum from SF_6-doped helium droplets.

scaled for display convenience—the total integrated intensity of each image is close to what is expected from the ion yields. Image a is the SF_5^+ fragment ion following dissociative ionization of gas-phase SF_6 at 25.5 eV. Images b and c are the corresponding droplet images following excitation at 25.5 and 21.8 eV, respectively. The next image, d, shows SF_5^+ after 22.8 eV excitation with the droplet beam on. It is shown with a logarithmic intensity scale, as the signal is very weak and almost not visible with a linear intensity scale. Photons of this energy sit in the "absorption gap" of pure helium droplets, where the pure helium droplet absorption has a minimum.[39] In this image, because the $SF_5^+{}_{drop}$ contribution is weak, the signal from the $SF_5^+{}_{gp}$ background is of comparable intensity, and a direct comparison of the $SF_5^+{}_{drop}$ and $SF_5^+{}_{gp}$ can be made. The $SF_5^+{}_{drop}$ image does not have the same center as $SF_5^+{}_{gp}$, a consequence of the entrainment of the SF_{6drop} in the helium beam, which has a well-defined laboratory velocity, versus the SF_{6gp} background, which has an average lab velocity near zero. One immediately sees differences between the $SF_5^+{}_{gp}$ and $SF_5^+{}_{drop}$ images. The radial extent of an image is directly related to the speed of the ion, so it is clear that $SF_5^+{}_{gp}$ ions are much faster than the $SF_5^+{}_{drop}$ ions. In addition, the $SF_5^+{}_{gp}$ images are anisotropic, while the $SF_5^+{}_{drop}$ angular distributions are isotropic. Additional images (not shown) were collected at other photon energies, both above and below the helium droplet absorption threshold. At all energies, the overall appearance of the SF_5^+ related to the droplet is similar to the ones shown.

In molecular photodissociation, one typically reports center-of-mass kinetic energy distributions, $P(E_k)$, derived from photofragment images, but in the droplet, some of the nearby He atoms may play a role in maintaining momentum conservation. As a result, momentum matching is not straightforward, and E_k cannot be determined unambiguously. Therefore, we report the fragment speed distributions $P(s)$ instead. Figure 8 displays $P(s)$ distributions for the SF_5^+ fragments following 25.5 eV excitation. Within the accuracy of the experiment, no significant differences were seen in the speed distributions from the $SF_5^+{}_{drop}$ images at different photon energies, so only the distributions following 25.5 eV excitation are shown. The $SF_5^+{}_{gp}$ speed distribution peaks far from zero, with an average speed $\langle s \rangle = 310 \pm 20$ m s^{-1} and a most probable speed slightly higher, at $\sim 350 \pm 20$ m s^{-1}. The distributions are quite different for the $SF_5^+{}_{drop}$. The ions are traveling much more slowly, with an average velocity of 115 ± 10 m s^{-1} and a most probable speed of 86 ± 6 m s^{-1}. Quantitative fitting of the angular distributions to the familiar expression for dissociation following absorption of linearly polarized light[42]—$f(\theta) = (1/(4\pi))\{1 + \beta P_2(\cos\theta)\}$—gives $\beta = 0.8$ for $SF_5^+{}_{gp}$ and $\beta = 0$ for $SF_5^+{}_{drop}$.

We also recorded velocity-mapped photoelectron images. Photoelectron spectra of SF_{6gp} and SF_{6drop} taken with 21.8 eV excitation energy are shown in Figure 9. The machine configuration in this experiment precluded the collection of full coincidence spectra, so the SF_{6drop} spectra are carefully background corrected. An image is taken with SF_6 in the pickup cell with the droplet beam on. Next, an image is taken while the cell is left on with the droplet beam blocked. Last, an image is taken with just a pure droplet beam. The two background images are then subtracted from the "all on" image with appropriate weighting. The pure droplet image is necessary because after excitation at 21.8 eV, the droplets fluoresce in the VUV. Some of these VUV photons directly strike the MCP or impinge upon metal surfaces within the spectrometer and

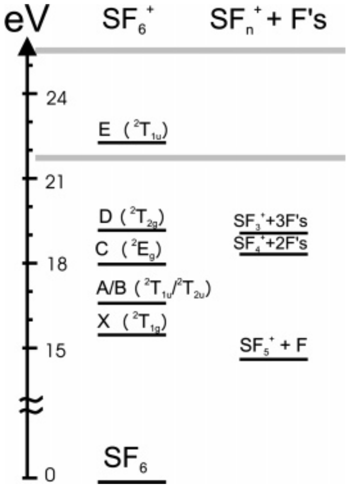

Figure 10. Energy level diagram for SF_6^+. Also shown are the thermodynamic thresholds for the formation of smaller SF_k^+ ions, assuming atomic F losses. The gray bars indicate the two excitation energies used in this study, 21.8 and 25.5 eV.

generate electrons, giving rise to a low-level dc background signal. Comparison of the TOF mass spectra taken with the helium beam on and off indicate exclusively SF_6-related differences, so we believe this procedure is robust and accurately reflects electrons from the cluster. Photoelectron spectra above the ionization energy (IE) of the helium atom were also recorded and appeared nearly identical to the pure droplet spectra collected by the authors, reflecting the fact that He ionization is much more likely than direct dopant ionization.

In the 21.8 eV photoelectron spectrum of SF_{6gp}, the fastest electrons comprising the small feature centered at 5.5 eV arise from ionization to the $\tilde{X}$ state of SF_6^+. The dominant feature, with electron kinetic energies (eK_E) centered near 4.5 eV eK_E, arises from ionization to the $\tilde{A}/\tilde{B}$ states of SF_6^+. The next two features, centered at 3.5 and 2.0 eV eK_E, arise from ionization to the $\tilde{C}$ and $\tilde{D}$ states, respectively.[35,43] All four features are seen in the photoelectron spectrum of SF_{6drop}. Within experimental resolution, peak positions are the same in the two spectra. The intensity pattern is quite different, however, with the peak corresponding to the $\tilde{A}/\tilde{B}$ states considerably less distinct for SF_{6drop}. Overall, there appears to be an underlying continuous contribution to the SF_{6drop} spectrum that is particularly visible below 1.2 eV. However, it does appear that the states accessed by photoionization of SF_{6gp} are all accessed by photoionization of SF_{6drop}. We note that previous work by Loginov et al.[5] showed that the photoelectron spectra of droplets doped with aniline were shifted by about 0.1 eV toward higher eK_E compared to those of bare aniline. We do not see such a shift, but a shift of this size would be difficult to observe in any case owing to the broad nature of the features in Figure 9.

4. Discussion

The data from SF_6-doped helium droplets show many interesting features. First, the ion yield spectra for SF_5^+ from droplets show strong features not present in the gas-phase SF_6 spectra. The spectra appear to match the absorption spectra of pure helium droplets, indicating strong coupling of excitation and/or ionization of the droplet with the SF_6 dopant, similar to what was seen for droplets doped with rare gas atoms.[24] Second, the modification in the shape of the ion yield comes about as a result of greatly increased SF_5^+ signal with almost no concomitant changes in SF_3^+ and SF_4^+. The photoelectron images from SF_6-doped droplets show, however, that SF_6^+ is being created in the droplet in the $\tilde{C}$ and $\tilde{D}$ states, states known for bare SF_6 to result in extensive fragmentation to SF_k^+, $k = 3,4,5$.[43] This poses the question of what effect helium environment has on the fragmentation process, and as a corollary, how the helium dissipates energy and at what rate.

Additionally, the ion imaging results give direct evidence that the SF_5^+ ion is interacting strongly with the droplet. The departing SF_5^+ fragment is significantly slowed as it escapes. Also, most of the SF_5^+ coming from the droplets is bare, with only a small fraction leaving with attached helium atoms. The images also show the SF_5^+ is slowed similarly in the droplet for all excitation energies, raising the issue of what role, if any, the initial excitation plays in the escape dynamics. As excitation and subsequent transfer of energy to the dopant is the first step in all of the processes described above, we will begin the discussion here.

4.A. Excitation Transfer Processes. In most optical studies on doped helium droplets,[1,44,45] the helium environment is completely transparent to the incoming photon. Photoabsorption of the droplet itself does not occur at excitation energies below ~21 eV, so any absorption in this regime must arise from the dopant. Above 21 eV, the helium is no longer transparent—the droplet environment undergoes electronic excitation which can then migrate to the dopant. In this section, we will examine the different processes responsible for dopant ionization within the droplet.

For excitation below 23 eV, the apparent threshold for ionization in He droplets,[26] neutral species are the only possible energy carrier. In our experiments, we excite the droplet optically, injecting a well-defined amount of energy. Although there is strong broadening and some symmetry breaking,[39−41] the simplified picture of 21.8 eV irradiation is that photoabsorption is a perturbed atomic $^1S-^1P$ excitation. In time-resolved fluorescence work on both bulk liquid helium and helium droplets,[46] strong VUV emission was seen from the droplets within 10 ns, implying fully allowed radiative transitions.

This inference is important, because in the Penning process leading to dopant ionization, two transitions can be active: one involving electron exchange, the other an optical-like electronic dipole interaction.[47,48] In "traditional" Penning processes, a high-energy, long-lived metastable state is created and collides with a partner, leading to ionization. A prerequisite for "long-lived" is that the excited molecule or atom does not have a dipole-allowed transition to its ground state. As such, the dipole component of these reactions is very weak, and electron exchange dominates.

If the excitation carrier remains in a state that has a dipole-allowed transition to the ground state, the cross section for Penning ionization by the dipole−dipole mechanism will be considerably larger than by electron exchange.[48] The distinction between the two ionization mechanisms is relevant to our experiment, because electron exchange usually results in the formation of ions with a distribution of final states different than from optical excitation.[49] For ionization via the dipole mechanism, the nascent ion distribution should resemble that created by direct photoionization. Our photoelectron spectrum for SF_{6drop} at 21.8 eV (Figure 9), which shows only minor differences when compared to that of bare SF_6, thus supports Penning ionization of the SF_6 dopant via the dipole mechanism.

For excitation with photon energies above the ionization energy of atomic helium, the most probable initial event is ionization of a helium atom within the droplet. Fast resonant charge hopping subsequently occurs, with the excitation migrating through the droplet. The charge either localizes, forming molecular helium ions, or it encounters the dopant and undergoes charge transfer, ionizing the dopant. The efficiency of charge transfer to the dopant has been previously examined in the groups of Janda[21,22] and Miller[50] for droplets doped with rare gas atoms and HCN, respectively. The results from Lewis et al.,[50] using a novel experimental method combining state selective infrared spectroscopy and electron impact ionization, suggested that the overall efficiency of the process is affected mainly by the electrostatic potential between the dopant and the migrating charge. As the droplet size increased, the likelihood of charge transfer decreased; there is an increased chance for the migrating charge to localize first to He_2^+, after which the droplet is expected to fragment explosively. For droplets of $\sim 10^4$ atoms, the charge-transfer probabilities were estimated to be 20−40% for the dopants studied.

In the charge-transfer experiments of Ruchti et al.,[21] the efficiencies were slightly lower but followed the same trend with droplet size. The overall efficiency of charge transfer also appeared to increase with the polarizability of the dopant. In our experiment, we can estimate the efficiency of the charge-transfer process with a few (perhaps crude) assumptions. First, we estimate the ratio of pure to doped droplets from the expected droplet size distributions generated from our beam source and the known pickup conditions in our gas cell. Next, we assume that all of the helium droplets that absorb a 25.5 eV photon ionize *and* fragment into species that we detect with equal efficiency (<1200 amu and $\tau_{frag} < 10\ \mu s$), regardless of whether they contain a dopant. By dividing the total ion counts for He_n-related signal by the total ion counts for the SF_6-related signal, and comparing this to the ratio predicted above by our source conditions, we find charge transfer is quite facile, with efficiencies of 70 ± 30%. Further studies are underway in our group to investigate charge transfer in other systems and experimentally refine the assumptions used in the estimating the charge-transfer probabilities.

4.B. SF_6 Fragmentation. In our TOF-MS results at 21.8 eV we see a large enhancement of SF_5^+, with no apparent effect on the production of smaller ions. With photon energies of 25.5 eV, there is also a very large preponderance for SF_5^+ creation, but some smaller SF_k^+ ions are created within the droplet. Here, we examine the apparent suppression of SF_k^+ ions in more detail and attempt to understand the underlying causes of the differences in fragmentation in these two energy regimes.

Before examining the changes in fragmentation of SF_6^+ *within* the droplet at these different energies, it is helpful to recall the energetics and fragmentation dynamics of SF_{6gp}. Figure 10 shows the energy levels of the SF_6^+ ion and the thresholds for the SF_k^+ ($k = \{5,4,3\}$) assuming sequential loss of F atoms.[51,52] Excitation into all of the SF_6^+ ionic states leads to dissociation, with the $\tilde{X}$, $\tilde{A}$, $\tilde{B}$ states producing SF_5^+ only. These states ($\tilde{X}$, $\tilde{A}$, $\tilde{B}$) are purely repulsive—at the $\tilde{X}$ state threshold, ~1 eV of translational energy is deposited into the departing fragments—leading to ejection of a fluorine atom on a subpicosecond time scale.[32,34,38] The $\tilde{C}$ and $\tilde{D}$ states result in three fragment ions: SF_5^+, SF_4^+, and SF_3^+, with the SF_5^+ dominating the yields and the smaller fragment ions thought to result from the unimolecular decomposition of internally excited SF_5^+ fragments.[32] The $\tilde{E}$ state appears to lead exclusively to SF_3^+ fragments.[53]

We first point out that the droplet photoelectron spectrum at 21.8 eV shows that states of bare SF_6^+ known to decay into smaller SF_k^+ fragments are being created in the droplet. Regardless of any possibility of altered electronic dynamics, all of the possible SF_6^+ states produced will fragment. Because the translational dynamics appear unchanged with varying photon energy, as in the gas-phase SF_6 dissociative ionization,[32] the excess energy left after the electron departs must be deposited into SF_5^+ internal excitation. This is critical for interpreting the changes in the fragmentation dynamics, because if the excitation greatly favored directly producing SF_6^+ ion in any of its three lowest lying states, with the electron removing the all of the excess energy, only SF_5^+ could be produced, so the lack of the smaller SF_k^+ ions would not be surprising. The helium droplet would have affected the *production* of the ions directly, and no *cooling* would be necessary.

From the ion yield curve in Figure 2, we know that droplet photoionization at 21.8 eV results primarily in SF_5^+ production, with very little SF_4^+ and SF_3^+ observed. Further insight into the ion fragmentation dynamics can be gained from the TOF-MS data in Figure 6. At 21.8 eV, the SF_5^+ peak from droplet photoionization is much narrower than that from photoionization of gas-phase SF_6. This result reflects the much slower speed distribution of SF_5^+ produced from the droplet, as discussed in more detail below with reference to the photofragment imaging results. No such narrowing is seen for SF_4^+ or SF_3^+ at 21.8 eV; we take this to mean that this photoionization signal does not arise from droplets at all but instead originates from background SF_6 in the ionization region. Fragmentation of SF_5^+ is thus nearly completely suppressed in our droplets at 21.8 eV.

At 25.5 eV excitation, the situation is slightly different, in that the TOF-MS peaks for SF_4^+ and SF_3^+ when the droplet beam is on also exhibit narrowing, indicating they are indeed formed from photoionization of doped droplets. The presence of the $SF_3^+{\cdot}He_n$ progression (Figure 5) at 25.5 eV (but not at 21.8 eV) directly supports this conclusion. Hence, there appears to be more (but still very weak) fragmentation of SF_5^+ at 25.5 eV than at 21.8 eV. Two factors contribute to this observation. The first is simple energetics. At 21.8 eV, the maximum possible available energy for SF_6^+ is 6.5 eV ($E_{h\nu} - IE_{dopant}$), while at 25.5 eV the available energy is given by $E_{avail} = IE_{He} - IE_{dopant} = 9.3$ eV. The extent of energy removal needed to suppress fragmentation is less, because the thresholds for formation of SF_4^+ and SF_3^+ are ~3.2 and ~3.6 eV above the SF_6 ionization energy, respectively.[52,54] Hence, the droplet environment must dissipate ~3.3 (2.9) and ~6.1 (5.7) eV internal energy for excitation at 21.8 and 25.5 eV, respectively, to suppress fragmentation to SF_4^+ (SF_3^+).

From both the images and the TOF data, the departing SF_5^+ has similar speeds at 21.8 and 25.5 eV, so it does not appear that the additional energy at 25.5 eV is going into translation. In the gas phase, none of the valence excited states of SF_6^+ decay radiatively, so it does not seem probable that this mechanism is prominent in the droplet. The energy must go into the internal energy of the SF_6^+. At 25.5 eV, for SF_5^+ production to be dominant, and the other SF_k^+ to be completely suppressed, over 6 eV of energy must be dissipated to the local environment. The appearance of the smaller ions may then reflect the greater difficulty of removing this excess energy quickly enough.

The second contributing factor is that at 25.5 eV excitation, charge transfer can populate the $\tilde{E}$ electronic state, which in the gas phase leads exclusively to SF_3^+ products. In gas-phase measurements following $\tilde{E}$ state excitation, the SF_3^+ fragment has substantial kinetic energy, and the dissociation is thought to be direct.[32] If the $\tilde{E}$ state were populated, direct formation of SF_3^+ in the droplet is expected to occur, and its detection would be inevitable. Note that in the TOF spectra, the width of the SF_3^+ peak, though narrowed compared to the gas-phase width,

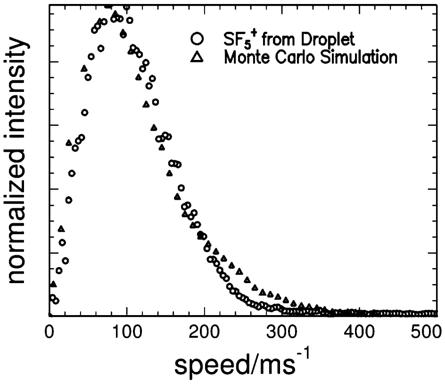

Figure 11. Comparison of measured $SF_5{}^+{}_{drop}$ speed with the result of the Monte Carlo simulation with $\sigma \approx 50$ Å^2.

is not as noticeably narrowed as the $SF_4{}^+$, and it is tempting to speculate that the different TOF width reflects the different dynamics involved in the production of $SF_3{}^+$.

4.C. $SF_5{}^+$ Escape. On the basis of the results for SF_{6gp}, the $SF_5{}^+$ fragment is formed with $\langle s \rangle \approx 300$ m s^{-1},[32] well above the Landau critical velocity. For SF_{6drop}, the average velocity of the escaping $SF_5{}^+$ fragments is also ~2 times greater than the Landau velocity. For these fast moving particles in the droplet it is unlikely that the more esoteric properties of the fluid play significant roles in the escape dynamics. We can then ignore any subtleties of the $SF_5{}^+$−helium interaction and analyze the escape process using a simple collisional energy transfer model as a first-order approximation to the system.

The results of Braun and Drabbels[12,55] on the escape of neutral photofragments from the interior of helium droplets were interpreted using a classical Monte Carlo simulation. The core of this simulation relies on the scattering of hard spheres, but it adds several opportune features. First, the broad size distribution of the clusters is taken into account, as is the initial position of the dopant and the evaporative loss of helium atoms from the droplet following pickup. Additionally, from the best fit of the model to the experiment, an effective hard-sphere collision cross section is determined and can be critiqued for physicality. The experimental results of Braun and Drabbels were simulated successfully by this procedure.[12] We have used the same simulation program to examine our data.

The Monte Carlo simulation does a reasonable job of fitting our experimental results. The speed distributions fit quite well, with an effective collision cross section of ~50 ± 10 Å^2 (Figure 11). The simulations also give the collision number and escape time distributions for the fragments, as well as an overall probability for escape. For fragments starting with the gas-phase mean velocity, the collisional distribution gives a maximum number of collisions of ~60 with an average number of collisions of ~30. The average escape time, $\langle \Delta\tau_{drop} \rangle$, is ~25 ps. The simulations indicate the probability of escape for the $SF_5{}^+$ fragment is <99.99%, consistent with the absence of $SF_6{}^+$ in the mass spectrum. If the $SF_5{}^+$ and the F were both trapped in the droplet, the pair would be bound by the ion-induced dipole attraction. In our experiments, though we observe no $SF_6{}^+$, we observe $SF_5{}^+\cdot$He, a system that is expected to be more weakly bound because of the lower polarizability of helium. We conclude that all ionization events lead to prompt fragmentation, and to the escape of at least one of the fragments, so that no recombination can occur. The simple hard-sphere collision model thus agrees with the experimental observations, both in our ionic dissociative ionization results and in the neutral dissociation results of Braun and Drabbels.[12] This agreement lends strength to the validity of using the Monte Carlo simulations to describe the collision dynamics of moving particles, both neutrals and ions, in helium droplets.

The angular distributions derived from the simulations do not fit the experiment as well as the speed distributions. If we use the gas-phase anisotropy value as an input parameter, the output distributions are not isotropic, with the simulated images remaining slightly anisotropic for the higher speed fragment ions. This behavior is consistent with both theoretical and experimental work that show that the angular anisotropy should relax more slowly than the kinetic energies.[56−58] However, we feel that the lack of agreement between the recorded angular distributions and those of the simulation does not indicate that the model is poor. Instead, the disparate results probably arise from the indirect nature of the dopant ionization mechanism. The SF_6 does not interact with the ionizing photon, but instead, with either He* or He$^+$ created by that photon. It is therefore reasonable to expect memory of the light polarization to be lost as the excitation or charge migrates through the droplet.

A priori, it was not obvious that the Monte Carlo simulations would give reasonable results for $SF_5{}^+$. In the CF_3I system studied by Braun and Drabbels,[12] the resulting interaction between the *neutral* CF_3 and He is expected to be weak, the result of a dipole-induced dipole interaction. This weak interaction supports the use of a simple collision theory to model the escape of the photofragments. In our system, photoabsorption results in the formation of $SF_6{}^+$ which then dissociates on a subpicosecond time scale into $SF_5{}^+$ and F. The $SF_5{}^+$ fragment is charged and will have a much stronger interaction with the local helium environment. Theoretical studies of ions in liquid helium indicate the formation of a “snowball”; the strong electrostriction leads to a great increase in helium density, frozen around the ionic core. If the outgoing particle were dragging many helium atoms with it, we would expect significant modification of its ballistic properties. However, the TOF-MS results show that most of the $SF_5{}^+$ escapes bare, with no helium attached, and the simulation gives results that match the measured velocity distributions. This, of course, does not mean that there is no attractive potential between the $SF_5{}^+$ and the helium, only that the dynamics of escape in this finite system do not allow the overall system to relax and reach equilibrium with the environment before it escapes.

4.D. Cooling Process. The combination of TOF-MS and ion imaging gives crucial information for directly determining the rate of cooling in the droplet. The highly repulsive initial dissociation event is likely still very fast, <1 ps, so ion escape from the droplet determines the time scale of droplet−ion interaction. The Monte Carlo simulations of the escape then give the average time spent in the droplet by the $SF_5{}^+$, $\langle \Delta\tau_{drop} \rangle$. From the strongly altered ion branching ratios, internal energy $\langle E_{lost} \rangle$ must be dissipated in the droplet to prevent fragmentation; this value is known from the discussion in section 4.B. A lower limit to the cooling rate is then given by $\langle E_{lost} \rangle / \langle \Delta\tau_{drop} \rangle \approx 3 \times 10^{15}$ K s^{-1}. The actual *total* rate of energy dissipation in the helium droplet is slightly higher, because the translational energy of the $SF_5{}^+$ and F are not included, though the maximum possible translational energy that could be deposited from $SF_6{}^+$ dissociation is ~1.5 eV and does not significantly alter the results.

This cooling rate is consistent with the ones that can be estimated from suppression of unimolecular decomposition of the $SF_5{}^+$. At 25.5 eV excitation the dissociation rate is expected to be ~10^{10} to 10^{11} s^{-1}. From this value, the cooling rate in the droplet must be on the order of 1×10^{15} K s^{-1}. A similar value was estimated by Lewis et al. based on another ion, triphenyl methanol.[25] Note, however, that the cooling rates calculated from the rate constant suffer from a large uncertainty because of the difficulties in estimating rate constants in these systems. Thus the "direct" method is much more robust.

With energy transfer rates of $\sim 10^{15}$ K s^{-1}, the cooling of ions is quite efficient in helium droplets, with multiple eVs of energy being dissipated in picoseconds. Theoretical predictions for the cooling of vibrationally excited He_2^+ are also quite high, up to an order of magnitude higher than those reported here.[59,60] In neutral species, vibrational relaxation has been seen to be about 1 order of magnitude slower for static species[61,62] and appears even slower for photofragments formed with significant recoil velocity.[55] One effect altering the cooling rates for neutral species versus ions in helium droplets is that, for the neutral, the strongest possible interaction between the droplet and the dopant is a dipole-induced dipole attraction, and this is only possible for polar species. For the ion, the ion-induced dipole interaction is the weakest attraction, and this already is typically much stronger and of longer range. It may simply be that for the ions, the much stronger interaction with the droplet environment induces much faster relaxation.

The actual mechanism for the droplet to dissipate the energy is still not conclusively known and would benefit greatly from more theoretical work. For droplets of our size ($\langle 10^4 \rangle$ atoms), >80% of the atoms would be evaporated if the cooling were an equilibrium process, i.e., if each He atom evaporated with nearly zero translational energy. It would be difficult to reconcile our escape results with a process involving several thousand individual evaporation events, as the number of fragment collisions is low and the time spent in the droplet small. Additionally, preliminary data in our group indicates little change in the branching ratio of the ionic fragments for smaller droplets, where the energy loss required to suppress fragmentation exceeds the nominal heat capacity of the droplet given by thermal evaporation. This suggests that the energy dissipation mechanism is far from a thermal process, and large amounts of energy are taken away by relatively few helium atoms. Similar results have been seen for static ions in the Miller group,[25] where they found that the cooling rate in the helium droplets was extremely nonlinear with droplet size, with the first few thousand atoms lost removing the bulk of energy.

5. Conclusion

We have investigated the photoionization and photofragmentation dynamics of He nanodroplets doped with single SF_6 molecules using tunable vacuum ultraviolet radiation from the Advanced Light Source. We have measured mass spectra, photoelectron spectra, and photofragment images resulting from droplet photoionization. The photoion yield spectra show that dopant ionization occurs indirectly via excitation or charge exchange from the surrounding He atoms, in agreement with earlier measurements by Toennies' group[26] on this system and more recent work in our group[24] on droplets doped with rare gas atoms. The mass spectra show that no parent SF_6^+ is produced, that SF_5^+ is by far the dominant fragment, and that further fragmentation to SF_4^+ and SF_3^+ is suppressed in the droplet. This suppression is more complete at 21.8 eV and less so at 25.5 eV.

The photoelectron spectrum of SF_6-doped droplets at 21.8 eV is similar but not identical to that of gas-phase SF_6, indicating that the same set of SF_6^+ states, all of which are dissociative, are accessed in the droplet. Photofragment imaging of the SF_5^+ fragment shows significant slowing in the droplet compared to the photoionization of bare SF_6. The measured speed distribution can be modeled using a Monte Carlo simulation based on binary collisions between the SF_5^+ and droplet atoms. The suppression of SF_5^+ fragmentation in the droplet is attributed to extremely rapid cooling, with a rate estimated to be 10^{15} K s^{-1}.

Acknowledgment. This work was supported by the Director, Office of Science, Office of Basic Energy Sciences, Chemical Sciences Division of the U.S. Department of Energy under Contract No. DE-AC02-05CH11231. D.S.P. gratefully acknowledges Marcel Drabbels for providing the source code for the Monte Carlo simulations. J.H.K. gratefully acknowledges the Korea Science and Engineering Foundation (KOSEF) for a postdoctoral fellowship. D.M.N. is very grateful to Charles B. Harris for sharing many stimulating lunches over the last 20 years.

References and Notes

(1) Callegari, C.; Lehmann, K. K.; Schmied, R.; Scoles, G. *J. Chem. Phys.* **2001**, *115*, 10090.
(2) Miller, R. E. *Faraday Discuss.* **2001**, *118*, 1.
(3) Toennies, J. P.; Vilesov, A. F.; Whaley, K. B. *Phys. Today* **2001**, *54*, 31.
(4) Peterka, D. S.; Lindinger, A.; Poisson, L.; Ahmed, M.; Neumark, D. M. *Phys. Rev. Lett.* **2003**, *91*, 043401.
(5) Loginov, E.; Rossi, D.; Drabbels, M. *Phys. Rev. Lett.* **2005**, *95*, 163401.
(6) Barrera, R.; Baym, G. *Phys. Rev. A* **1972**, *6*, 1558.
(7) Gunther, H.; Foerste, M.; Putlitz, G. Z.; Schumacher, T. *Fiz. Nizk. Temp.* **1996**, *22*, 189.
(8) Foerste, M.; Guenther, H.; Riediger, O.; Wiebe, J.; Putlitz, G. Z. *Z. Phys. B: Condens. Matter* **1997**, *104*, 317.
(9) Scheidemann, A.; Schilling, B.; Toennies, J. P.; Northby, J. A. *Physica B* **1990**, *165*, 135.
(10) Harms, J.; Toennies, J. P. *Phys. Rev. Lett.* **1999**, *83*, 344.
(11) von Haeften, K.; Laarmann, T.; Wabnitz, H.; Moller, T. *Phys. Rev. Lett.* **2002**, *88*, 233401.
(12) Braun, A.; Drabbels, M. *Phys. Rev. Lett.* **2004**, *93*, 253401.
(13) Cole, M. W.; Bachman, R. A. *Phys. Rev. B* **1977**, *15*, 1388.
(14) Buzzacchi, M.; Galli, D. E.; Reatto, L. *Phys. Rev. B* **2001**, *64*, 094512.
(15) Atkins, K. R. *Phys. Rev.* **1959**, *116*, 1339.
(16) Gunther, H.; Foerste, M.; Kunze, M.; Putlitz, G. Z.; vonStein, U. *Z. Phys. B: Condens. Matter* **1996**, *101*, 613.
(17) Farnik, M.; Henne, U.; Samelin, B.; Toennies, J. P. *Z. Phys. D: At., Mol. Clusters* **1997**, *40*, 93.
(18) Farnik, M.; Samelin, B.; Toennies, J. P. *J. Chem. Phys.* **1999**, *110*, 9195.
(19) Scheidemann, A.; Schilling, B.; Toennies, J. P. *J. Phys. Chem.* **1993**, *97*, 2128.
(20) Callicoatt, B. E.; Forde, K.; Ruchti, T.; Jung, L.; Janda, K. C.; Halberstadt, N. *J. Chem. Phys.* **1998**, *108*, 9371.
(21) Ruchti, T.; Callicoatt, B. E.; Janda, K. C. *Phys. Chem. Chem. Phys.* **2000**, *2*, 4075.
(22) Ruchti, T.; Forde, K.; Callicoatt, B. E.; Ludwigs, H.; Janda, K. C. *J. Chem. Phys.* **1998**, *109*, 10679.
(23) Callicoatt, B. E.; Forde, K.; Jung, L. F.; Ruchti, T.; Janda, K. C. *J. Chem. Phys.* **1998**, *109*, 10195.
(24) Kim, J. H.; Peterka, D. S.; Wang, C. C.; Neumark, D. M. *J. Chem. Phys.* **2006**, *124*, 214301.
(25) Lewis, W. K.; Applegate, B. E.; Sztaray, J.; Sztaray, B.; Baer, T.; Bemish, R. J.; Miller, R. E. *J. Am. Chem. Soc.* **2004**, *126*, 11283.
(26) Frochtenicht, R.; Henne, U.; Toennies, J. P.; Ding, A.; Fiebererdmann, M.; Drewello, T. *J. Chem. Phys.* **1996**, *104*, 2548.
(27) Wiley, W. C.; McLaren, I. H. *Rev. Sci. Instrum.* **1955**, *26*, 1150.
(28) Whitaker, B. J. Image Reconstruction: The Abel Transform. In *Imaging in Chemical Dynamics*; Suits, A., Continetti, R. E., Eds.; American Chemical Society: Washington, DC, 2001; Vol. 770, p 68.
(29) Heck, A. J. R.; Chandler, D. W. *Ann. Rev. Phys. Chem.* **1995**, *46*, 335.
(30) Eppink, A.; Parker, D. H. *Rev. Sci. Instrum.* **1997**, *68*, 3477.
(31) Heimann, P. A.; Koike, M.; Hsu, C. W.; Blank, D.; Yang, X. M.; Suits, A. G.; Lee, Y. T.; Evans, M.; Ng, C. Y.; Flaim, C.; Padmore, H. A. *Rev. Sci. Instrum.* **1997**, *68*, 1945.
(32) Peterka, D. S.; Ahmed, M.; Ng, C. Y.; Suits, A. G. *Chem. Phys. Lett.* **1999**, *312*, 108.
(33) Creasey, J. C.; Jones, H. M.; Smith, D. M.; Tuckett, R. P.; Hatherly, P. A.; Codling, K.; Powis, I. *Chem. Phys.* **1993**, *174*, 441.

(34) Creasey, J. C.; Lambert, I. R.; Tuckett, R. P.; Codling, K.; Frasinski, L. J.; Hatherly, P. A.; Stankiewicz, M. *J. Chem. Soc., Faraday Trans.* **1991**, *87*, 1287.

(35) Yencha, A. J.; Thompson, D. B.; Cormack, A. J.; Cooper, D. R.; Zubek, M.; Bolognesi, P.; King, G. C. *Chem. Phys.* **1997**, *216*, 227.

(36) Mitsuke, K.; Suzuki, S.; Imamura, T.; Koyano, I. *J. Chem. Phys.* **1990**, *93*, 8717.

(37) Ono, M.; Mitsuke, K. *Chem. Phys. Lett.* **2003**, *379*, 248.

(38) Ono, M.; Mitsuke, K. *Chem. Phys. Lett.* **2002**, *366*, 595.

(39) Joppien, M.; Karnbach, R.; Moller, T. *Phys. Rev. Lett.* **1993**, *71*, 2654.

(40) Joppien, M.; Muller, R.; Moller, T. *Z. Phys. D: At., Mol. Clusters* **1993**, *26*, 175.

(41) von Haeften, K.; Laarmann, T.; Wabnitz, H.; Moller, T. *Phys. Rev. Lett.* **2001**, *87*, 153403.

(42) Zare, R. N. *Mol. Photochem.* **1972**, *4*, 1.

(43) Berkowitz, J. *Photoabsorption, Photoionization, and Photoelectron Spectroscopy*; Academic Press: New York, 1979.

(44) Hartmann, M.; Miller, R. E.; Toennies, J. P.; Vilesov, A. *Phys. Rev. Lett.* **1995**, *75*, 1566.

(45) Stienkemeier, F.; Vilesov, A. F. *J. Chem. Phys.* **2001**, *115*, 10119.

(46) von Haeften, K.; Laarmann, T.; Wabnitz, H.; Moller, T. *J. Phys. B: At. Mol. Opt. Phys.* **2005**, *38*, S373.

(47) Miller, W. H. *J. Chem. Phys.* **1970**, *52*, 3563.

(48) Ukai, M.; Yoshida, H.; Morishima, Y.; Nakazawa, H.; Shinsaka, K.; Hatano, Y. *J. Chem. Phys.* **1989**, *90*, 4865.

(49) Ohno, K.; Tanaka, H.; Yamakita, Y.; Maruyama, R.; Horio, T.; Misaizu, F. *J. Electron Spectrosc. Relat. Phenom.* **2000**, *112*, 115.

(50) Lewis, W. K.; Lindsay, C. M.; Bemish, R. J.; Miller, R. E. *J. Am. Chem. Soc.* **2005**, *127*, 7235.

(51) Evans, M.; Ng, C. Y.; Hsu, C. W.; Heimann, P. *J. Chem. Phys.* **1997**, *106*, 978.

(52) Fisher, E. R.; Kickel, B. L.; Armentrout, P. B. *J. Chem. Phys.* **1992**, *97*, 4859.

(53) Hitchcock, A. P.; Vanderwiel, M. J. *J. Phys. B: At. Mol. Opt. Phys.* **1979**, *12*, 2153.

(54) Cheung, Y. S.; Chen, Y. J.; Ng, C. Y.; Chiu, S. W.; Li, W. K. *J. Am. Chem. Soc.* **1995**, *117*, 9725.

(55) Braun, A. Photodissociation Studies of CH_3I and CF_3I in Fluid ^{4}Helium Nanodroplets. Ph.D. Dissertation, Ecole Polytechnique Federale de Lausanne, 2004.

(56) Shizgal, B.; Blackmore, R. *Chem. Phys.* **1983**, *77*, 417.

(57) Cline, J. I.; Taatjes, C. A.; Leone, S. R. *J. Chem. Phys.* **1990**, *93*, 6543.

(58) Chapman S.; Cowling, T. G. *The Mathematical Theory of Non-Uniform Gases*, 3rd ed.; Cambridge University Press: Cambridge, 1970.

(59) Scifoni, E.; Bodo, E.; Dellepiane, G.; Gianturco, F. A. *Eur. Phys. J. D* **2004**, *30*, 363.

(60) Seong, J.; Janda, K. C.; Halberstadt, N.; Spiegelmann, F. *J. Chem. Phys.* **1998**, *109*, 10873.

(61) Lindsay, C. M.; Miller, R. E. *J. Chem. Phys.* **2005**, *122*, 104306.

(62) Scheele, I.; Conjusteau, A.; Callegari, C.; Schmied, R.; Lehmann, K. K.; Scoles, G. *J. Chem. Phys.* **2005**, *122*, 104307.